

White-light emission of blue-luminescent graphene quantum dots by europium (III) complex incorporation



Sejung Kim^{a, b}, Joon Kyo Seo^a, Jun Hong Park^a, Youngjun Song^b, Ying Shirley Meng^b, Michael J. Heller^{b, c, *}

^a Materials Science Engineering, University of California San Diego, La Jolla, CA 92093, USA

^b Department of Nanoengineering, University of California San Diego, La Jolla, CA 92093, USA

^c Department of Bioengineering, University of California San Diego, La Jolla, CA 92093, USA

ARTICLE INFO

Article history:

Received 10 January 2017

Received in revised form

17 July 2017

Accepted 12 August 2017

Available online 13 August 2017

ABSTRACT

Traditionally, graphene quantum dots are prepared by fragmentation of graphene sheets into the nanoscale particles of controlled sizes followed by band gap adjustment by doping with electron-donating elements. Our novel synthetic aqueous arc discharge process has been developed to produce the blue-luminescent graphene quantum dots (bGQDs). The resulting bGQDs are ~15 nm in diameter and the amount of oxygen-including functional groups can be controlled to 27.4% and 30.8% at 1 and 4 A of a current level, respectively. The presence of a band gap is confirmed by using scanning tunneling microscopy/spectroscopy (STM/STS). Additionally, we investigated the effect of oxygen doping levels on the band gap by photoluminescence (PL) behaviors and a density functional theory (DFT). The PL emission is red-shifted from 397 to 425 nm corresponding to the amount of oxygen-including functional groups in bGQDs and the DFT calculation confirms the decrease in a band gap from ~2.0 to ~1.7 eV due to electron donation from oxygen. In addition, our quantum dots have promising applications for practical use in optoelectronics devices. For example, tris-dibenzoylmethane mono-1,10-phenanthroline-europium (III) ($\text{Eu}^{\text{III}}\text{DP}$) is incorporated with bGQDs for white-light emission and is shown to be successfully fabricated into light-emitting polymer films.

Published by Elsevier Ltd.

1. Introduction

Graphene has drawn much attention due to its versatile applications in energy generation/storage, electronic devices, and light-emitting devices, and has led to the development of various synthetic methods and applications for other two-dimensional (2D) nanostructures [1–6]. However, because of the zero band gap in graphene, band gap engineering in graphene has been limited for optoelectronic applications; therefore, the functionalization of graphene has been employed with covalent approaches. Among the various graphene derivatives, zero-dimensional (0D) graphene quantum dots (GQDs) have been reported as a new type of quantum dot that is composed of sp^2 carbon clusters surrounded by sp^3 carbons at a few-nanometers scale [7–10]. Due to the quantum confinement effect (QCE), the electronic and optical band gaps of

GQDs can be manipulated by either controlling the morphological features at the nanoscale level, such as size and width, or employing chemical doping with high electronic affinity elements like nitrogen [11–15]. Otherwise, the reduction processes of nanoscale graphene oxide have been found to be capable of engineering the band gap [7–9].

Photoluminescence (PL) and resonance energy transfer are highly desired results of band gap manipulation. In terms of the resonance energy transfer, white-light emission can be achieved by incorporating fluorophores with different PL emission wavelengths followed by balancing the emission intensity between fluorophores [16,17]. Similarly, white emissive GQD composites can also be achieved through functionalization of GQDs with biocompatible polymers, lanthanides or nanoparticles, wherein the intramolecular distance can be adjustable corresponding to environmental conditions such as pH, temperature, and metal ions [18–20]. In our previous study, we show that the seamless aqueous arc discharge process we developed can produce graphene sheets with controllable degrees of oxidation by adjusting the arc

* Corresponding author. Department of Nanoengineering, University of California San Diego, La Jolla, CA 92093, USA.

E-mail address: mheller@ucsd.edu (M.J. Heller).

discharge power [21–23]. Here, we present the fine modulation of GQDs band gap by introducing different amounts of oxygen-including functional groups according to the arc discharge power. The presence of the band gap is confirmed by using scanning tunneling microscopy (STM) and scanning tunneling spectroscopy (STS). The change in the band gap of GQDs is investigated by photoluminescence (PL) behaviors for the different oxygen doping levels and density functional theory (DFT) calculations. The resonance energy transfer of blue-luminescent GQDs (bGQDs) is not only investigated by incorporating a luminescent europium (III) embedded organic complex to obtain white emission, but also fabricated into light emitting polymer films to show it as a promising platform material for potential optoelectronic applications.

2. Experimental

2.1. Synthesis of bGQDs by an arc discharge in water

A high purity of graphite is used for the cathode (6 mm in diameter, 99.999%, Aldrich) and anode (12 mm in diameter, 99.999%, Aldrich). The seamless arc discharge in DI water (18.2 M Ω) is operated by moving the anode up and down to contact the fixed cathode on the bottom and a discharge is initiated by applying a voltage (25 V). The arc discharge power is controlled by tuning the current to either 1 or 4 A during the arc discharge process. The plasma zone produced between the two graphite electrodes heats the surface of the graphite, which induces the exfoliation of graphene from the graphite electrodes with simultaneous pressure fluctuation of water. The graphene particles were collected using vacuum filtration and re-dispersed in organic solvents such as *N*-methyl-2-pyrrolidone (NMP) and dimethylformamide (DMF) followed by ultrasonication. The nanometer-sized GQDs were obtained by centrifugation at 7000 rpm for 30 min.

2.2. Computation methodology

The first principles calculations are carried out based on the spin-polarized generalized gradient approximation (GGA) using the Perdew-Burke-Ernzerhof (PBE) exchange correlation as parameterized in the Vienna ab initio simulation package (VASP) [24,25]. We use a plane-wave basis set and the projector-augmented wave (PAW) method [26,27]. In all calculations, C ($2s^2 2p^2$), H ($1s^1$), and O ($2s^2 2p^4$) are treated as the valence electron configurations. A gamma point is specified in the Brillouin zone, and periodic boundary conditions are imposed on the unit cell where a vacuum size is twice as large as a GQD's diameter to prohibit interactions among the images. We use a cutoff energy of 1.3 times the maximum cutoff specified by the pseudopotential of oxygen. The electronic energy difference is set to be required for convergence to 10^{-4} eV. All the atoms are fully relaxed to simulate the optimized structure. The density of states (DOS) for structurally optimized GQDs is calculated using the Gaussian smearing.

2.3. Characterization

The morphological features of bGQDs were observed using scanning electron microscopy (ESEM, Philips XL30) operated at 10 kV and transmission electron microscopy (TEM, FEI Tacnai G2, Sphera) with an accelerating voltage of 200 kV. The height distribution of bGQDs was determined by atomic force microscopy (AFM, Dimension 3100 Veeco) with a tapping mode by using a Si tip (resonance frequency = 320 kHz; spring constant = 42 N/m). X-ray photoelectron spectroscopy (XPS) measurements for the elemental analysis of bGQDs were performed on an AXIS Supra (Kratos) photoelectron spectrometer. The Raman spectra were collected

with a 532 nm laser using a Reinschaw inVia Raman Microscope. The UV–vis spectra and PL emission spectra were collected using a Shimadzu UV-3600 spectrometer with a correction for the solvent background and a fluorescence spectrophotometer (PerkinElmer, LS-55). STM and STS was performed in an ultra-high vacuum chamber (6×10^{-11} torr), using Omicron VT (variable temperature). To obtain STM images and STS, electrochemical etched tungsten tips were employed.

3. Results and discussion

3.1. Preparation of bGQDs by an aqueous arc discharge

The bGQDs are produced by the aqueous arc discharge and the detailed synthetic procedure is demonstrated in the [Experimental section](#). As shown in Fig. 1a, once the voltage is applied at different currents (1 and 4 A at 25 V, called bGQDs1A and bGQDs4A, respectively) to graphite electrodes, a plasma zone is produced in the gap between the electrodes (inset of Fig. 1a-ii), which heats the surface of the graphite electrodes. The heating of the plasma zone induces thermal expansion of graphite, after which water molecules are intercalated between each graphene layer, resulting in the exfoliation of graphene sheets from the graphite electrodes. Subsequently, the produced graphene moves towards the water surface and assembles into thin graphene-based membranes (inset of Fig. 1a-i and Fig. S1). Fig. 1b shows a representative transmission electron microscopy (TEM) image of bGQDs1A, which has a diameter of ~15 nm, and bGQDs4A is shown in Fig. S2. Fig. 1c displays the representative height profile obtained from an atomic force microscopy (AFM) image showing the transferred bGQDs1A on a SiO₂ substrate; the line trace is obtained from the A-B of AFM images. As a result, the average height obtained is 3.69 ± 1.54 nm and 2.80 ± 1.76 nm for bGQDs1A and bGQDs4A (Fig. S2), respectively.

To elucidate the electronic structure of synthesized bGQDs, the local density of states (LDOS) of bGQDs is determined by scanning tunneling microscopy (STM) and spectroscopy (STS). As shown in Fig. 1d, isolated bGQDs1A with ~15 nm diameter are transferred to a highly ordered pyrolytic graphite (HOPG), similar to that for AFM images. The LDOS of bGQDs is compared to the LDOS of a bare HOPG terrace using STS, which has been employed by Ogawa, Banin and Ritter et al. in determining electronic structures of semiconductor quantum dots [28–30]. As shown in the differential conductivities in STS, the bare HOPG has zero band gap structure with V-shaped LDOS. Conversely, the LDOS of both HOMO and LUMO in bGQDs decreases as shown by the arrow, and a finite band gap can be observed, consistent with oxidation. It is noted that this measured LDOS could be combined with non-emissive organic components, because STM tips can receive tunneling signal from both GQDs and other organic molecules. Solvent-only deposited HOPG is also investigated by STM and STS in Fig. S3 as a control.

3.2. Photoluminescence mechanism of bGQDs

The bGQDs1A and bGQDs4A dispersion in *N*-methyl-2-pyrrolidone (NMP) have blue-light emission under UV lights at 366 nm shown in Fig. 2. The bGQDs1A has a strong peak at 397 nm and an absorption band at 305 nm (blue arrow). Meanwhile, the PL emission of bGQDs4A is red-shifted by 28 nm compared to that of bGQDs1A. The bGQDs4A has a PL emission at 425 nm when excited at 340 nm with a full width at half maximum (FWHM) of about 100 nm which is a common value of carbon-based quantum dots [31,32]. The PL excitation (PLE) of bGQDs1A and bGQDs4A has 334 nm and 340 nm, respectively, as shown in Fig. S4. It is noticed that the differences between absorption and PLE peak of bGQDs1A might result from the internal conversion process due to the

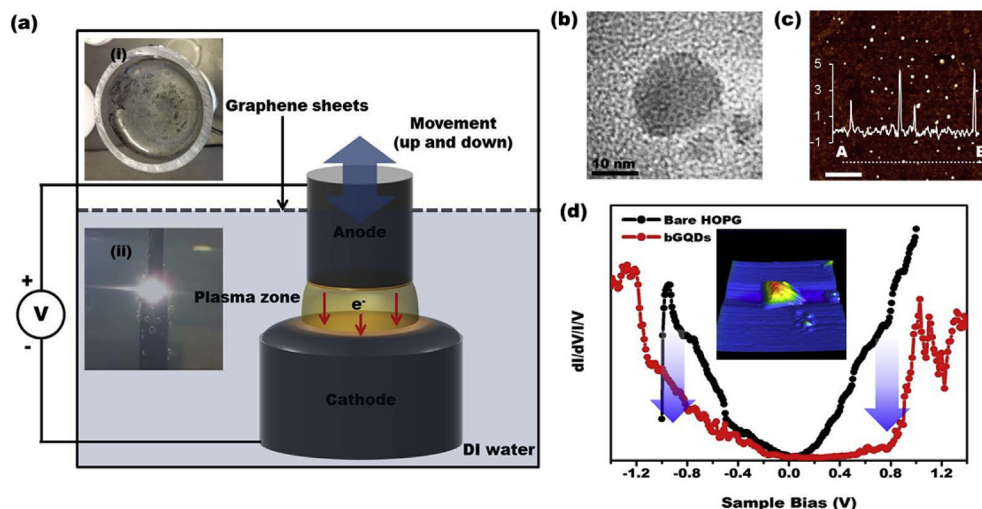


Fig. 1. Production of bGQDs through the seamless arc discharge in water. a) Schematic illustration of the seamless arc discharge in water to produce bGQDs shows the vertical movement of the anode, the fixed cathode, and water used as a dielectric medium. a-i) Graphene sheet-based films on the water surface formed by self-assembly of the graphene produced from the exfoliation of graphite electrodes. a-ii) A digital photo image of the plasma zone during the arc discharge process produced by applying 25 V with either 1 or 4 A. b) A representative TEM image of bGQDs1A after purification by centrifugation at 6000 rpm for 30 min c) An AFM image of bGQDs1A on a silicon wafer for determination of height profiles with the inset of a representative height profile of A-B (scale bar: 500 nm). d) STS results show the presence of a ~ 1.8 eV band gap (represented by arrows) of bGQDs1A (red) compared to HOPG (0 eV); inset: STM image of bGQDs1A. (A colour version of this figure can be viewed online.)

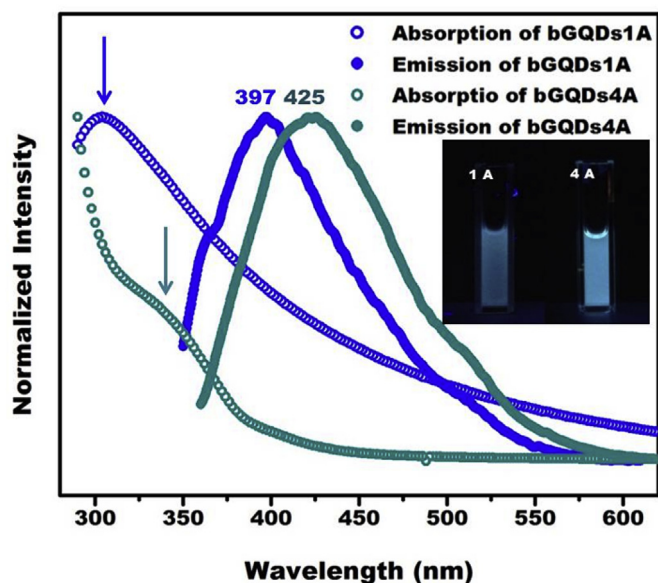


Fig. 2. The UV-vis absorption and PL emission of bGQDs1A (blue open- and filled circles) and bGQDs4A (light blue open- and filled circles) and blue-light emission of bGQDs under UV light at 366 nm. (A colour version of this figure can be viewed online.)

chemical composition changes [8,34]. The excitation- and solvent-dependent PL emission behavior could be affected by the structural rearrangements of solvent molecules on the surface of bGQDs due to the solvent relaxation process for bGQDs [30]. The carbon-based quantum dots have an excitation wavelength-dependent emission due to the time-dependent processes involved. The ratio of the emission to excitation wavelength ($\Delta\lambda_{em}/\Delta\lambda_{ex}$) is constant due to the time-dependent emission energy of solvent relaxation [9]. In bGQDs dispersions, upon excitation of the fluorophore (bGQDs), the change in the dipole moment of bGQDs and solvent molecules leads to the rearrangement of surrounding solvent molecules in order to lower the energy of the excited bGQDs (solvent relaxation). During the relaxation process from the fluorophore-solvent excited

state, the solvent relaxation process is completed before the bGQDs emission because of the relaxation time difference between common polar solvents (~ 10 ps) and fluorophores (a few nanoseconds), which leads to a red-shift of fluorescence. Therefore, the solvation process for PL emission plays an important role in peak shifts.

In Fig. 3, the bGQDs display excitation-dependent emission wavelength behaviors. The PL emission of bGQDs1A exhibits a strong peak at 397 nm when excited at 340 nm. The maximum peak position moved to 520 nm by sweeping through excitation wavelengths in increments of 20 nm up to 410 nm. Moreover, the bGQDs4A have an excitation wavelength-dependent emission in Fig. 3b. They have a strong emission peak at 425 nm when excited at 330 nm, and the maximum peak position moves to 460 nm with increasing the excitation wavelengths by 20 nm increments. In our bGQDs, the emission peak of bGQDs1A in NMP is at 430 nm under an excitation of 340 nm. However, it was red-shifted to 520 nm under an excitation of 420 nm. Aside from the excitation wavelength dependency, the red-shifted PL emission of bGQDs is observed in the polar solvent due to strong solvent-bGQDs interactions, while the shape of the fluorescence of bGQDs was broadened and blue-shifted in toluene due to fewer interactions shown in Fig. 3c. The solvent relaxation effects on peak shifts were investigated in a non-polar solvent (toluene) and another polar solvent (DMF). In general, however, the QDs PL emission is dependent on the excitation wavelength and solvents, which does not follow Kasha's rule in that the PL peak position of QDs is not dependent on the excitation wavelength [33,34].

Due to the uniform distribution in sizes of bGQDs, it is assumed that the 28 nm red-shifted PL emission of bGQDs4A is directly due to a change in the chemical composition of bGQDs during the arc discharge process followed by a change in the band gap. X-ray photoemission spectroscopy (XPS) is carried out to elucidate the effect of oxygen doping on bGQDs. Fig. 4a and b shows the high-resolution XPS spectra of C1s for bGQDs, which verifies the presence of oxygenated carbon and determines the relative quantities of carbon in different functional groups. Fig. 4a shows that bGQDs1A are mostly composed of C=C (284.6 eV, blue), consistent with a 72.65% relative content ratio. The remaining chemical bonding configurations are assigned to oxygen-containing

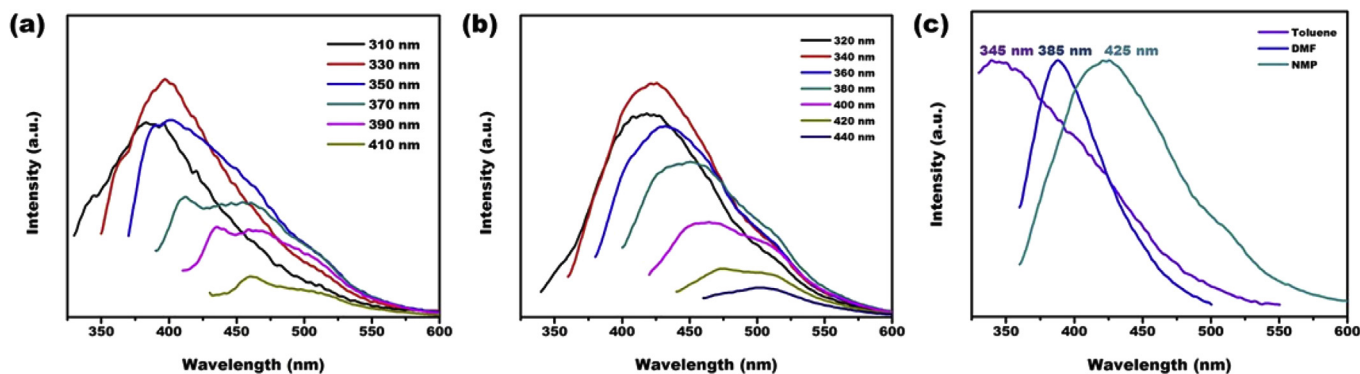


Fig. 3. Excitation wavelength-dependent PL spectra in increments of 20 nm of (a) bGQDs1A and (b) bGQDs4A. (c) Solvent-dependent PL spectra of the bGQDs1A in organic solvents, toluene (violet), DMF (blue), and NMP (light-blue). (A colour version of this figure can be viewed online.)

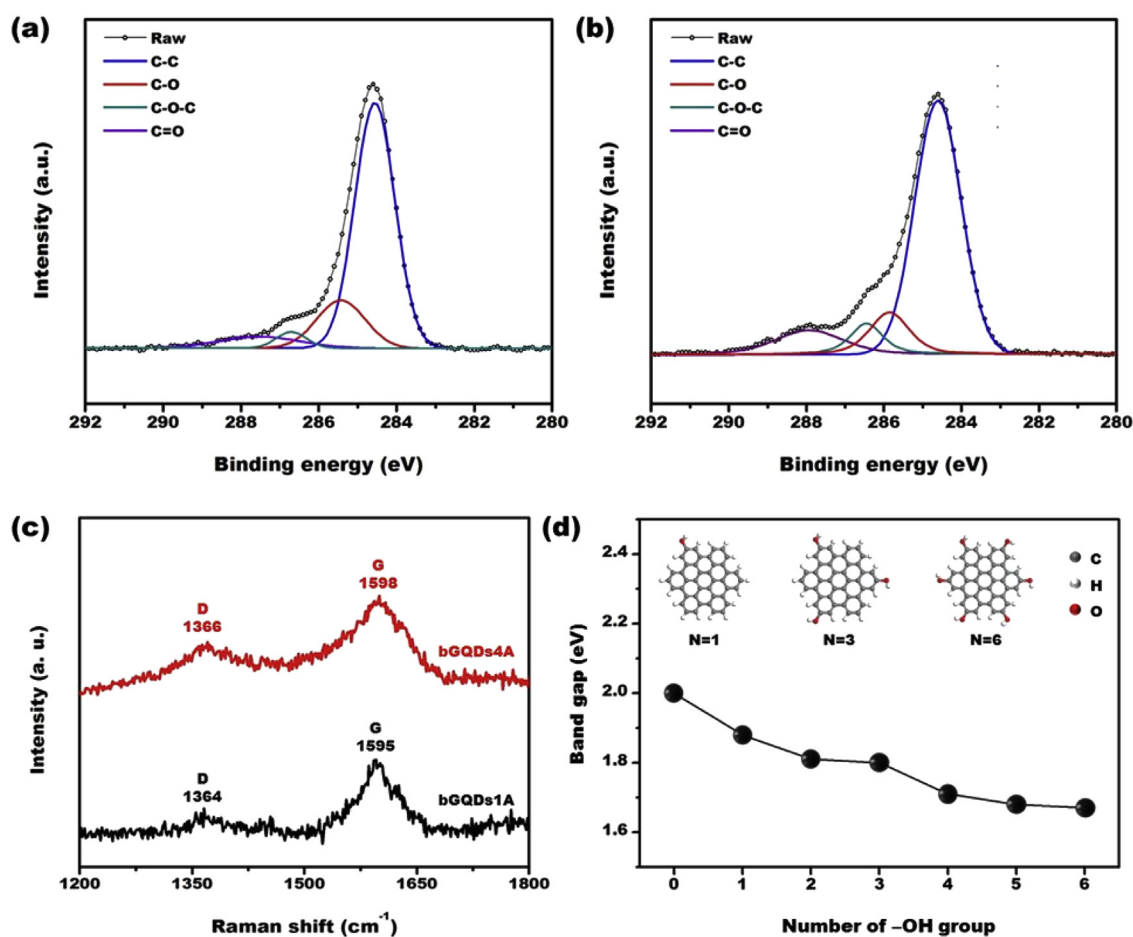


Fig. 4. Physicochemical characterization of bGQDs. a) and b) XPS analysis of bGQDs1A and bGQDs4A, respectively, shows that the change in the number of oxygen-including functional groups is dependent on the arc discharge power. c) Raman spectroscopy analysis of bGQDs1A (black) and bGQDs4A (red) shows the quality of the graphitic structure resulting from the different amounts of oxygen. d) Band gap change with respect to the number of $-OH$ adsorption. (A colour version of this figure can be viewed online.)

functional groups C–O (285.7 eV, red), C–O–C (286.5 eV, green), and C=O (287.7 eV, purple) and the relative contents of each bonding type were found to be 17.07%, 3.54%, and 6.74%, respectively. In Fig. 4b, the deconvolution of XPS C1s spectra obtained from bGQDs4A indicates the presence of oxygen-containing functional groups and their relative contents are C=C (284.6 eV, blue, 69.23%), C–O (285.7 eV, red, 11.71%), C–O–C (286.5 eV, green, 7.73%), and C=O (287.8 eV, purple, 11.32%) bonds. Elemental

analysis using XPS confirmed the degree of oxidation of bGQDs during the aqueous arc discharge, which is dependent on the arc discharge power and leads to higher oxidation corresponding to current levels.

We also investigated the effect of introducing different amounts of oxygen on the quality of graphitic structures by Raman spectroscopy, as shown in Fig. 4c. The quality of the graphitic structure of the bGQDs is evaluated by comparing the relative intensities of

the D-band (1365 cm^{-1}) and G-band (1596 cm^{-1}), which represent the disorder and the crystalline structure of graphitic nanoparticles, respectively [35–37]. In Fig. 4c, the bGQDs1A has a D-band of 1364 cm^{-1} and a G-band of 1595 cm^{-1} , and the relative intensity of I_D/I_G is around 0.33. In addition, the bGQDs4A has a D-band of 1366 cm^{-1} and a G-band of 1598 cm^{-1} , which are upshifted 2 and 3 cm^{-1} compared to bGQDs1A, and the relative intensity of I_D/I_G is around 0.48. Although both relative intensities of I_D/I_G for both bGQDs are similar to that of high quality multilayered graphene, bGQDs4A has a slightly larger I_D/I_G than that of bGQDs1A, indicating bGQDs4A has less graphitic crystalline phase than bGQDs1A [14,35–37]. The Raman spectroscopy analyses show that the graphitic structure of bGQDs is influenced by the amount of oxygen doping. These results correspond to the results of elemental analysis by XPS, which lead to the limits of the π -conjugation system. In addition, the increase in the relative intensity of I_D/I_G was shown in our previous studies, which demonstrated that a larger arc discharge power results in higher oxygen doping levels [21–23]. Therefore, we conclude that by changing the power applied, the aqueous arc discharge process can adjust the chemical composition of the bGQDs that leads to band gap modulation, which is directly shown in the change in PL emission wavelength, as shown in Fig. 4a.

In order to validate our seamless process to control the amount of doped oxygen and the corresponding band gap change, the density of states (DOS) of bGQDs is studied by DFT calculations. It has been reported that sp^3 carbon bindings (defects) in QGDs separate sp^2 carbon clusters and PL emission originates from these isolated sp^2 carbon clusters [9,14,15]. It is assumed that our bGQDs are composed of isolated sp^2 carbon clusters within the sp^3 carbon matrix. For simplicity, we built a computational model of $1\text{ nm } sp^2$ clusters consisting of 13 aromatic rings where hydrogen (H) and hydroxyl ($-OH$) bind to carbon atoms around the edge (the inset of Fig. 4d). The DOS demonstrates that the band gap of QGDs with 6OH (C:O = 0.875:0.125) is $\sim 1.7\text{ eV}$. This value is similar to the band gap of bGQDs1A ($\sim 1.8\text{ eV}$ shown in Fig. 1d) composed of C:O = 0.857:0.143, which is a comparable ratio to the computational model of QGDs with 6OH. Interestingly, it is confirmed that the band gap of QGDs decreases as the oxygen doping levels increase: The HOMO is maintained at 0 eV with respect to Fermi level, but the LUMO declines with increasing doped oxygen levels (Fig. S5). In Fig. 4d, the band gap of $1\text{ nm } sp^2$ cluster model without $-OH$ group shows $\sim 2.0\text{ eV}$ that reduces to $\sim 1.7\text{ eV}$ when the model has 6OH. It is known that functional groups donate electrons to the antibonding state in the benzene ring, which leads to the reduction of the band gap in bGQDs [15]. Therefore, it is expected that the electrons are released from $-OH$ toward bGQDs and the band gap decreases as the number of $-OH$ increases.

The PL emission of QGDs is affected by the size of sp^2 carbon clusters at a few-nanometers scale; the relative composition ratio of sp^2 and sp^3 carbon bonding results in the change in π -conjugation length due to the isolation of sp^2 clusters by sp^3 -bonded carbons [7–10]. Subsequently, the band gap of the QGDs gradually decreases by increasing the amount of doped oxygen, which results in a red-shift of the PL emission due to the donation of electrons from external elements. However, the bGQDs produced by our aqueous arc discharge have a larger diameter ($\sim 15\text{ nm}$) composed of hundreds of benzene rings with infinite π -conjugation lengths and decreased band gap. According to the XPS results, the bGQDs have oxygen-including functional groups such as hydroxyl ($-OH$) at the edges and epoxy groups (C–O–C) in the basal plane. Furthermore, during the synthetic process, the relative amounts of oxygen-including functional groups are increased at the higher current (4 A), which is observed by a red-shifted PL emission. Therefore, it can be concluded that the band gap of bGQDs is largely affected by

the oxygen doping levels during the arc discharge process, resulting in a controlled the band gap according to arc discharge power.

3.3. bGQDs nanocomposites

Due to the long-lived and narrow bandwidth luminescence properties, lanthanide complexes have drawn attention in optoelectronic devices. In particular, a europium (III) complex, tris-dibenzoylmethane mono-1, 10-phenanthroline-europium (III) ($\text{Eu}^{\text{III}}\text{DP}$), can be conjugated with graphitic nanoparticles for luminescent carbon-based nanostructures [38]. Therefore, our luminescent bGQDs composed of sp^2/sp^3 carbons are assumed to be conjugated, leading to energy transfer between bGQDs and $\text{Eu}^{\text{III}}\text{DP}$ followed by emission color changes. The TEM image of the bGQDs- $\text{Eu}^{\text{III}}\text{DP}$ nanocomposite is shown to be irregularly aggregated, as shown in Fig. 5a. It is assumed that the nanocomposite aggregates are formed by conjugation of sp^2 carbons of bGQDs with phenanthroline in $\text{Eu}^{\text{III}}\text{DP}$ and negatively charged bGQDs also stabilize the aggregates. In addition, Raman spectrum shows the presence of europium complex in bGQDs- $\text{Eu}^{\text{III}}\text{DP}$ nanocomposites, as shown in Fig. S8. It is noted that the Raman spectra of the bGQDs- $\text{Eu}^{\text{III}}\text{DP}$ nanocomposites is comparable to that of carbon nanotubes and europium ion composites [38].

The emission color is changed from blue to red and white-light emission is observed, as shown in Fig. 5b. The PL emission behavior of the bGQDs- $\text{Eu}^{\text{III}}\text{DP}$ complex is investigated and showed blue emission of the bGQDs at 415 nm and red emission of $\text{Eu}^{\text{III}}\text{DP}$ at 598 and 613 nm (Fig. S6). In order to elucidate PL emission wavelength change, the PL emission spectra of the bGQDs- $\text{Eu}^{\text{III}}\text{DP}$ complex are investigated. Fig. 5c demonstrates the typical blue emission of bGQDs at 415 nm and red emission of the Eu^{III} ion with a dominant peak at 613 nm, with no detected emission peak at 596 nm. Excitation of the bGQDs- $\text{Eu}^{\text{III}}\text{DP}$ complex at 340 nm stimulates the blue emission and red emission at 415 nm and 613 nm, respectively. In Fig. 5c and Fig. S6, the increase in emission intensity of $\text{Eu}^{\text{III}}\text{DP}$ is shown with increasing amounts of $\text{Eu}^{\text{III}}\text{DP}$, and the emission color has been shifted to white emission.

In the bGQDs- $\text{Eu}^{\text{III}}\text{DP}$ complex system, the overlap of absorption spectra of bGQDs and $\text{Eu}^{\text{III}}\text{DP}$ at 340 nm weakened the short wavelength of emission at 415 nm due to energy transfer, and as a result, the longer wavelength at 613 nm is comparatively strengthened as shown in Fig. S6. The absorption and PLE peaks of only $\text{Eu}^{\text{III}}\text{DP}$ are shown in Fig. S7, which demonstrates the spectral overlap between bGQDs and $\text{Eu}^{\text{III}}\text{DP}$. In this regard, the white-light emission is probably attributed to the equilibrium of these emission intensities from bGQDs and $\text{Eu}^{\text{III}}\text{DP}$ rather than simple spectral overlap. The relative emission intensity of the bGQDs- $\text{Eu}^{\text{III}}\text{DP}$ complex of I_{613}/I_{415} when excited at 340 nm is increased from 0.016 to 0.43 with increasing $\text{Eu}^{\text{III}}\text{DP}$ concentration up to 200 μM , as shown in the inset of Fig. 5c. Thus, the energy transfer process of the complex acts as emission equilibrium for white-light emission.

The tunable light-emitting colors indicate that bGQDs nanocomposites can be used as emitting materials or promising dopant components for white-light-emitting diodes. Therefore, the versatile applications of bGQDs are investigated through fabrication of different forms in order to explore the promising candidates as light-emitting components. Fig. 5d shows a light-emitting film composed of the bGQDs- $\text{Eu}^{\text{III}}\text{DP}$ complex and poly(methylmethacrylate) (PMMA) used as a supporting material due to its high transparency. Here, the bGQDs- $\text{Eu}^{\text{III}}\text{DP}$ composite film is transparent under sunlight and the UC San Diego seal can be seen through the composite films (Fig. S9). The blue-, red- and white-emitting composite films are also demonstrated under UV light at 366 nm as shown in Fig. 5d. In addition, the bGQDs- $\text{Eu}^{\text{III}}\text{DP}$ nanocomposite-based light-emitting diode (LED) is fabricated by a

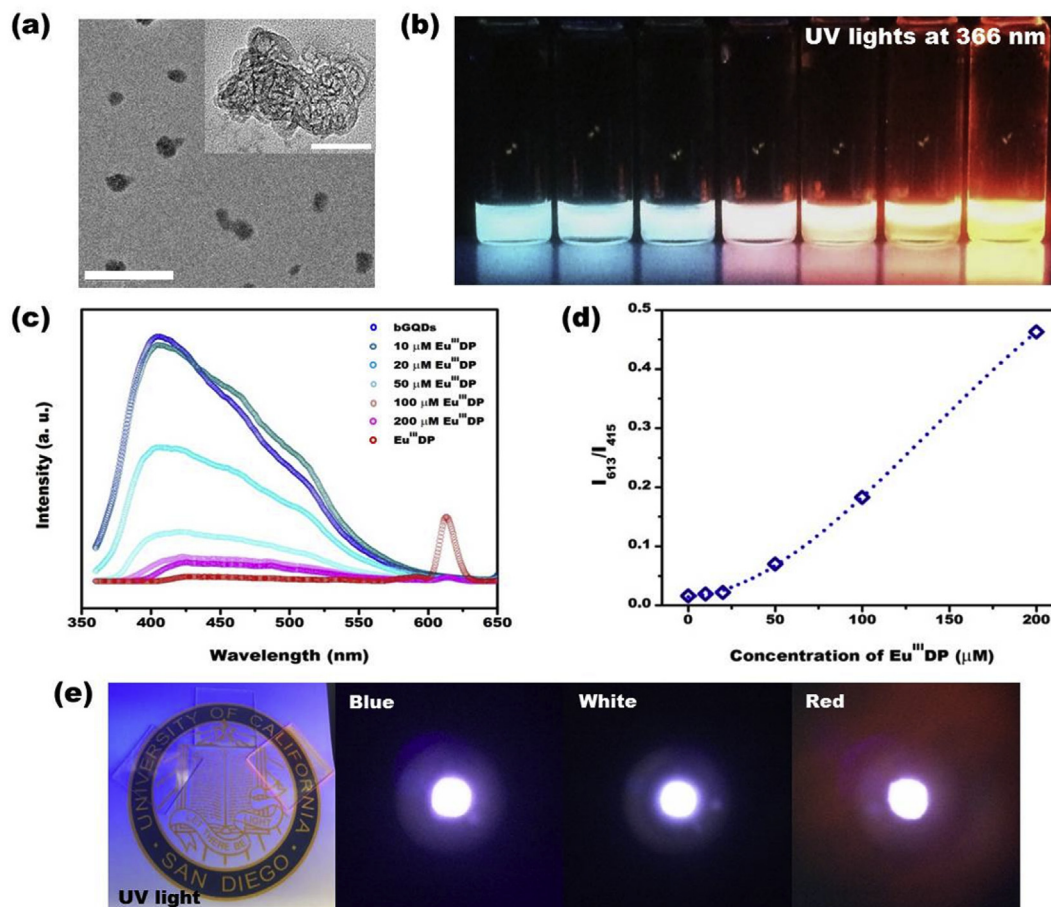


Fig. 5. a) A TEM image of the bGQDs-Eu^{III}DP complex aggregates (scale bar: 200 nm and 50 nm in the inset). b) A digital photo image of the change in PL emission color of the bGQDs-Eu^{III}DP complexes in DMF with concentrations of 0, 10, 20, 50, 100, 200 μM of Eu^{III}DP and only Eu^{III}DP from left to right. c) The PL emission spectra of the bGQDs-Eu^{III}DP complexes. d) The relative intensity of I_{613}/I_{415} according to the Eu^{III}DP complex onto bGQDs corresponding to (c). e) Light-emitting polymer films composed of the bGQDs-Eu^{III}DP complex and PMMA under UV light at 366 nm and the different color emissions from the construction of an LED by coating on a commercial blue LED (366 nm). (A colour version of this figure can be viewed online.)

simple solvent evaporation process to construct the white-emission diode and the schematic diagram of the LED we fabricated is shown in Fig. S6. As the color in light-emitting polymer films is changed by the increase in the amounts of Eu^{III}DP, the constructed LED emits blue, white, and red light. The tunability of the emission colors of the bGQDs-Eu^{III}DP complex shows our process as a promising candidate for achieving white-color emission through π - π interactions between two different color-emitting fluorophores. Furthermore, the resonance energy transfer of the bGQDs-Eu^{III}DP complex is shown to be an effective way to balance the PL emission intensity for desired color emissions.

4. Conclusions

In conclusion, our blue emission graphene quantum dots (bGQDs) with tunable photoluminescence (PL) emission are produced by controlling the degree of oxidation through an aqueous arc discharge process. The physicochemical structures are analyzed using Raman spectroscopy and XPS, which indicate that the bGQDs have high graphitic structure and that the oxygen doping levels of these bGQDs can be tunable as a function of the arc discharge power. The Eu^{III}DP complex is conjugated with bGQDs through π - π interactions to obtain the capability of emitting white color. The bGQDs-Eu^{III}DP complex emits a white color through resonance energy transfer that was successfully fabricated into light-emitting

polymer films. Hence, we have shown the versatility of the aqueous arc discharge process as a novel synthetic method capable of producing graphene-based white color emission fluorophores.

Acknowledgements

This research was supported by University of California, San Diego Heller Lab Royalty Fund BNGTTLB. The authors are grateful for Dr. Jennifer Wright and Dr. Adam Wright for fruitful discussions.

Appendix A. Supplementary data

Supplementary data related to this article can be found at <http://dx.doi.org/10.1016/j.carbon.2017.08.021>.

References

- [1] S. Stankovich, D.A. Dikin, G.H.B. Dommett, K.M. Kohlhaas, E.J. Zimney, E.A. Stach, et al., Graphene-based composite materials, *Nature* 442 (2006) 282–286.
- [2] K.H. Park, D. Lee, J. Kim, J. Song, Y.M. Lee, H.-T. Kim, et al., Defect-free, size-tunable graphene for high-performance lithium ion battery, *Nano Lett.* 14 (2014) 4306–4313.
- [3] K.S. Novoselov, A.K. Geim, S.V. Morozov, D. Jiang, Y. Zhang, S.V. Dubonos, et al., Electric field effect in atomically thin carbon films, *Science* 306 (2004) 666–669.
- [4] F. Xia, D.B. Farmer, Y. Lin, P. Avouris, Graphene field-effect transistors with high on/off current ratio and large transport band gap at room temperature,

- Nano Lett. 10 (2010) 715–718.
- [5] K.J. Koski, Y. Cui, The new skinny in two-dimensional nanomaterials, *ACS Nano* 7 (2013) 3739–3743.
- [6] X. Zhuang, Y. Mai, D. Wu, F. Zhang, X. Feng, Two-dimensional soft nanomaterials: a fascinating world of materials, *Adv. Mater.* 27 (2015) 403–427.
- [7] B. Pan, J. Zhang, Z. Li, M. Wu, Hydrothermal route for cutting graphene sheets into blue-luminescent graphene quantum dots, *Adv. Mater.* 22 (2010) 734–738.
- [8] F. Liu, M.-H. Jang, H.D. Ha, J.-H. Kim, Y.-H. Cho, T.S. Seo, Facile synthetic methods for pristine graphene quantum dots and graphene oxide quantum dots: origin of blue and green luminescence, *Adv. Mater.* 25 (2013) 3657–3662.
- [9] G. Eda, Y.-Y. Lin, C. Mattevi, H. Yamaguchi, H.-A. Chen, I.-S. Chen, et al., Blue photoluminescence from chemically derived graphene oxide, *Adv. Mater.* 22 (2010) 505–509.
- [10] L. Wang, S.-J. Zhu, H.-Y. Wang, S.-N. Qu, Y.-L. Zhang, J.-H. Zhang, et al., Common origin of green luminescence in carbon nanodots and graphene quantum dots, *ACS Nano* 8 (2014) 2541–2547.
- [11] A.K. Geim, K.S. Novoselov, The rise of graphene, *Nat. Mater.* 6 (2007) 183–191.
- [12] S. Kim, S.W. Hwang, M.-K. Kim, D.Y. Shin, D.H. Shin, C.O. Kim, et al., Anomalous behaviors of visible luminescence from graphene quantum dots: interplay between size and shape, *ACS Nano* 6 (2012) 8203–8208.
- [13] M.A. Sk, A. Ananthanarayanan, L. Hunag, K.H. Lim, P. Chen, Revealing the tunable photoluminescence properties of graphene quantum dots, *J. Mater. Chem. C* 2 (2014) 6954–6960.
- [14] T. Gokus, R.R. Nair, A. Bonetti, M. Böhmler, A. Lombardo, K.S. Novoselov, et al., Making graphene luminescent by oxygen plasma treatment, *ACS Nano* 3 (2009) 3963–3968.
- [15] S.H. Jin, D.H. Kim, G.H. Jun, S.H. Hong, S. Jeon, Tuning the photoluminescence of graphene quantum dots through the charge transfer effect of functional groups, *ACS Nano* 7 (2013) 1239–1245.
- [16] K.V. Rao, K.K.R. Datta, M. Eswaramoorthy, S.J. George, Highly pure solid-state white-light emission from solution-processable soft-hybrids, *Adv. Mater.* 25 (2013) 1713–1718.
- [17] Y. Chen, M. Zheng, Y. Xiao, H. Dong, H. Zhang, J. Zhuang, et al., Self-quenching-resistant carbon-dot powder with tunable solid-state fluorescence and construction of dual-fluorescence morphologies for white light-emission, *Adv. Mater.* 28 (2016) 312–318.
- [18] G. He, D. Guo, C. He, X. Zhang, X. Zhao, C.A. Duan, Color-tunable europium complex emitting three primary colors and white light, *Angew. Chem. Int. Ed.* 48 (2009) 6132–6135.
- [19] K. Paek, H. Yang, J. Lee, J. Park, B.J. Kim, Efficient colorimetric pH sensor based on responsive polymer-quantum dot integrated graphene oxide, *ACS Nano* 8 (2014) 2848–2856.
- [20] C.H. Park, H. Yang, J. Lee, H.-H. Cho, D. Kim, D.C. Lee, et al., Multicolor emitting block copolymer-integrated graphene quantum dots for colorimetric simultaneous sensing of temperature, pH, and metal ions, *Chem. Mater.* 27 (2015) 5288–5294.
- [21] S. Kim, Y. Song, T. Takahashi, T. Oh, M.J. Heller, An aqueous single reactor arc discharge process for the synthesis of graphene nanospheres, *Small* 11 (2015) 5041–5046.
- [22] S. Kim, Y. Song, J. Wright, M.J. Heller, Graphene bi- and trilayers produced by a novel aqueous arc discharge process, *Carbon* 102 (2016) 339–345.
- [23] S. Kim, Y. Song, S. Ibsen, S.-Y. Ko, M.J. Heller, Controlled degrees of oxidation of nanoporous graphene filters for water purification using an aqueous arc discharge, *Carbon* 109 (2016) 624–631.
- [24] G. Kresse, J. Furthmüller, Efficient Interactive Schemes for ab initio total-energy calculations using a plane-wave basis set, *Phys. Rev. B* 54 (1996) 11169–11186.
- [25] J.P. Perdew, K. Burke, M. Ernzerhof, Generalized gradient approximation made simple, *Phys. Rev. Lett.* 77 (1996) 3865–3868.
- [26] P.E. Blöchl, Projector augmented-wave method, *Phys. Rev. B* 50 (1994) 17953–17979.
- [27] G. Kresse, D. Joubert, From ultrasoft pseudopotentials to the projector augmented-wave method, *Phys. Rev. B* 59 (1999) 1758–1775.
- [28] S. Ogawa, F.-R.F. Fan, A.J. Bard, Scanning tunneling microscopy, tunneling spectroscopy, and photoelectrochemistry of a film of Q-CdS particles incorporated in a self-assembled monolayer on a gold surface, *J. Phys. Chem.* 99 (1995) 11182–11189.
- [29] U. Banin, Y.W. Cao, D. Katz, O. Millo, Identification of atomic-like electronic states in indium arsenide nanocrystal quantum dots, *Nature* 400 (1999) 542–544.
- [30] K.A. Ritter, J.W. Lyding, The influence of edge structure on the electronic properties of graphene quantum dots and nanoribbons, *Nat. Mater.* 8 (2009) 235–242.
- [31] H. Tetsuka, R. Asahi, A. Nagoya, K. Okamoto, I. Tajima, R. Ohta, et al., Optically tunable amino-functionalized graphene quantum dots, *Adv. Mater.* 24 (2012) 5333–5338.
- [32] C.-T. Chen, S.-S. Li, W.-J. Lai, Y.-C. Yeh, H.-A. Chen, I.-S. Chen, et al., Tunable photoluminescence from graphene oxide, *Angew. Chem. Int. Ed.* 51 (2012) 6662–6666.
- [33] M. Li, S.K. Cushing, X. Zhou, S. Guo, N. Wu, Fingerprinting photoluminescence of functional groups in graphene oxide, *J. Mater. Chem.* 22 (2012) 23374–23379.
- [34] S.K. Cushing, M. Li, F. Huang, N. Wu, Origin of strong excitation wavelength dependent fluorescence of graphene oxide, *ACS Nano* 8 (2014) 1002–1013.
- [35] C.-J. Shih, A. Vijayaraghavan, R. Krishnan, R. Sharma, J.-H. Han, M.-H. Ham, et al., Bi- and tri-layer graphene solutions, *Nat. Nanotechnol.* 6 (2011) 439–445.
- [36] Q.-Q. Li, X. Zhang, W.-P. Han, Y. Lu, W. Shi, J.-B. Wu, et al., Raman spectroscopy at the edges of multilayer graphene, *Carbon* 85 (2015) 221–224.
- [37] A.C. Ferrari, J.C. Meyer, V. Scardaci, C. Casiraghi, M. Lazzeri, F. Mauri, et al., Raman spectrum of graphene and graphene Layers, *Phys. Rev. Lett.* 97 (2006), 187401.
- [38] G. Accorsi, N. Armaroli, A. Parisini, M. Meneghetti, R. Marega, M. Prato, et al., Wet adsorption of luminescent Eu^{III} complex on carbon nanotubes sidewalls, *Adv. Funct. Mater.* 17 (2007) 2975–2982.